

# **Microwave Imaging of Buried Targets through a Multi-Zooming Approach: Reconstruction Capabilities for Different Object Conductivities**

M. Salucci, L. Poli, and A. Massa

## **Abstract**

In this work, the performance of an innovative microwave imaging methodology for buried object detection are analyzed. More precisely, the developed inverse scattering (*IS*) approach is based on a Multi-Frequency (*MF*) formulation of the buried *IS* equations in order to exploit the frequency diversity coming from wideband ground penetrating radar (*GPR*) measurements. The arising *MF* cost function is minimized through a customized deterministic solver based on a conjugate gradient (*CG*) minimizer nested within the iterative multi-scaling approach (*IMSA*) for achieving higher resolutions in the identified regions of interest (*RoIs*). Some illustrative numerical results are shown, in order to verify the effectiveness of the developed *MF-IMSA-CG* methodology when dealing with the retrieval of buried objects having different values of electric conductivity. For completeness, as well as for the sake of comparison, the reconstructions yielded by a competitive state-of-the-art approach based on a frequency hopping (*FH*) processing of the *GPR* spectrum are also shown, by considering several noise conditions.

# 1 Definitions

## 1.1 Glossary

- $D_{inv}$ : investigation domain;
- $D_{obs}$ : observation domain;
- $N$ : number of discretization cells in  $D_{ind}$ ;
- $V$ : number of views;
- $M$ : number of measurement points;
- $F$ : number of frequencies considered for the inversion;
- $(x_v, y_v)$ : coordinates of the  $v$ -th source ( $v = 1, \dots, V$ ).
- $(x_m^v, y_m^v)$ : coordinates of the  $m$ -th measurement point for the  $v$ -th view  $v$ , ( $m = 1, \dots, M$ );
- $\varepsilon_{ra} = \frac{\varepsilon_a}{\varepsilon_0}$ : relative electric permittivity for the upper half-space ( $y > 0$ );
- $\sigma_a$ : conductivity for the upper half-space ( $y > 0$ );
- $\varepsilon_{rb} = \frac{\varepsilon_b}{\varepsilon_0}$ : background relative electric permittivity;
- $\sigma_b$ : background conductivity;

## 2 Variation of the object conductivity

### 2.1 Square object ( $\varepsilon_{r,obj} = 6.0$ )

#### 2.1.1 Parameters

##### Background

Inhomogeneous and nonmagnetic background composed by two half spaces

- Upper half space ( $y > 0$  - air):  $\varepsilon_{ra} = 1.0$ ,  $\sigma_a = 0.0$ ;
- Lower half space ( $y < 0$  - soil):  $\varepsilon_{rb} = 4.0$ ,  $\sigma_b = 10^{-3}$  [S/m];

##### Investigation domain ( $D_{inv}$ )

- Side:  $L_{D_{inv}} = 0.8$  [m];
- Barycenter:  $(x_{bar}^{D_{inv}}, y_{bar}^{D_{inv}}) = (0.00, -0.4)$  [m];

##### Time-Domain forward solver ( $FDTD$ - $GPRMax2D$ )

- Side of the simulated domain:  $L = 6$  [m];
- Number of cells:  $N^{FDTD} = 750 \times 750 = 5.625 \times 10^5$ ;
- Side of the  $FDTD$  cells  $l^{FDTD} = 0.008$  [m];
- Simulation time window:  $T^{FDTD} = 20 \times 10^{-9}$  [sec];
- Time step:  $\Delta t^{FDTD} = 1.89 \times 10^{-11}$  [sec];
- Number of time samples:  $N_t^{FDTD} = 1060$ ;
- Boundary conditions: perfectly matched layer ( $PML$ );
- Source type: Gaussian mono-cycle (first Gaussian pulse derivative, called “Ricker” in  $GPRMax2D$ )
  - Central frequency:  $f_0 = 300$  [MHz];
  - Source amplitude:  $A = 1.0$  [A];

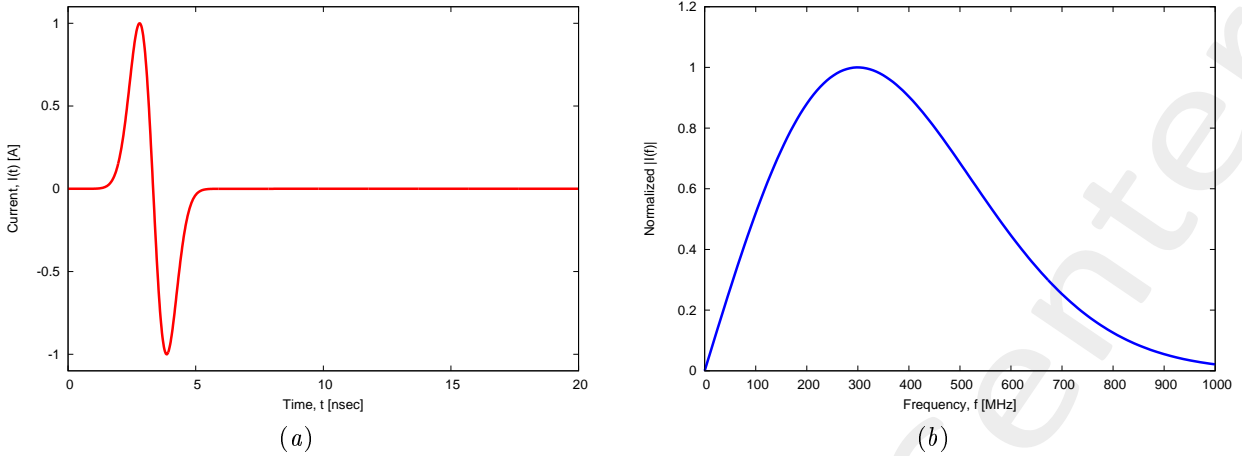


Figure 1: *GPRMax2D* excitation signal. (a) Time pulse, (b) normalized frequency spectrum.

### Frequency parameters

- Frequency range:  $f \in [f_{min}, f_{max}] = [200.0, 600.0]$  [MHz] [?] ( $-3$  [dB] bandwidth of the Gaussian Mono-cycle excitation centered at  $f_0 = 300$  [MHz]);
- Frequency step:  $\Delta f = 100$  [MHz] ( $F = 5$  frequency steps in  $[f_{min}, f_{max}]$ );

$f$ [MHz]	$\lambda_a$ [m]	$\lambda_b$ [m]	$f^*$ [MHz]
200.0	1.50	0.75	200.5
300.0	1.00	0.50	297.6
400.0	0.75	0.37	401.1
500.0	0.60	0.30	498.1
600.0	0.50	0.25	601.6

Table 1: Considered frequencies and corresponding wavelength in the upper medium ( $\lambda_a$ , free space) and in the lower medium ( $\lambda_b$ , soil).  $f^*$  is the nearest frequency sample available from transformed time-domain data, and represents the real frequency considered by the inversion algorithm.

### Scatterer

- Type: Square;
- Side: 0.16 [m];
- Electromagnetic properties:  $\epsilon_{r,obj} = 6.0$ ,  $\sigma_{obj} = \{10^{-4}; 5 \times 10^{-4}; 10^{-3}; 5 \times 10^{-3}; 10^{-2}\}$  [S/m];

$\epsilon_{r,obj}$	$\sigma_{obj}$ [S/m]	$\Re\{\tau\}$	$\Im\{\tau\}$
6.0	$10^{-4}$	2.0	$2.69 \times 10^{-2}$
6.0	$5 \times 10^{-4}$	2.0	$1.49 \times 10^{-2}$
6.0	$10^{-3}$	2.0	0.0
6.0	$5 \times 10^{-3}$	2.0	$-1.19 \times 10^{-1}$
6.0	$10^{-2}$	2.0	$-2.69 \times 10^{-1}$

Table 2: Real and imaginary parts of the contrast function vs. different values of object conductivity. The imaginary part is computed as  $\Im\{\tau\} = \left[ \frac{\sigma_b - \sigma_{obj}}{2\pi f \epsilon_0} \right]$  at the highest frequency ( $f_{max} = 600$  [MHz]).

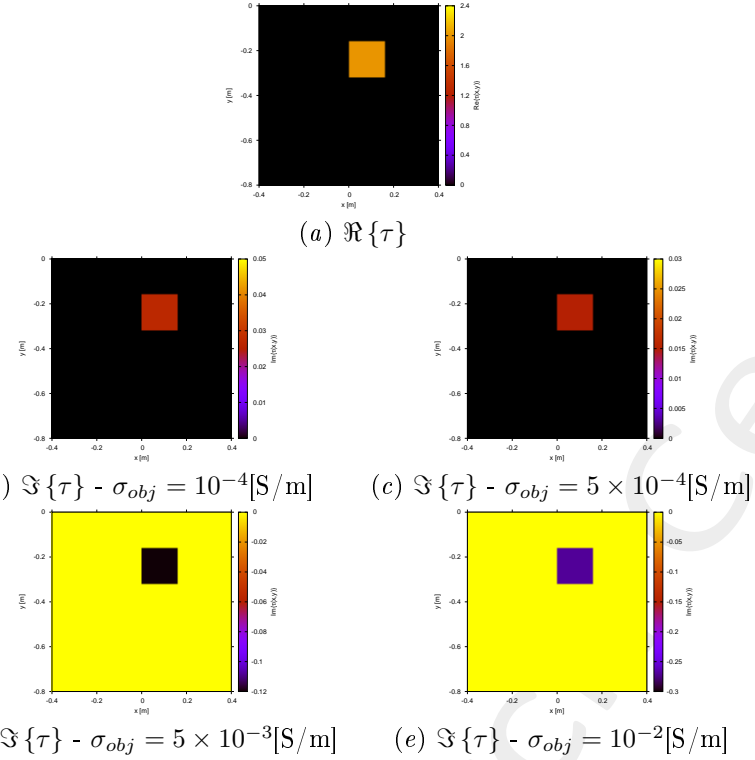


Figure 2: Actual object. The imaginary parts are plotted at  $f_{max} = 600$  [MHz].

### Measurement setup

- Considered frequency:  $f_{min} = 200$  [MHz],  $\lambda_b = 0.75$  [m].
- $\#DoFs = 2ka = \frac{2\pi}{\lambda_b}L\sqrt{2} = \frac{2\pi}{0.75}0.8\sqrt{2} \simeq 9.5$ ;
- Number of views (sources):  $V = 10$ ;
  - $\min\{x_v\} = -0.5$  [m],  $\max\{x_v\} = 0.5$  [m];
  - height:  $y_v = 0.1$  [m],  $\forall v = 1, \dots, V$ ;
- Number of measurement points:  $M = 9$ ;
  - $\min\{x_m\} = -0.5$  [m],  $\max\{x_m\} = 0.5$  [m];
  - height:  $y_m = 0.1$  [m],  $\forall m = 1, \dots, M$ ;

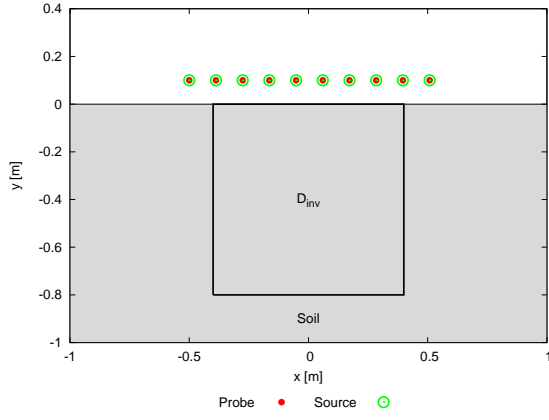


Figure 3: Location of the measurement points ( $M = 9$ ) and of the sources ( $V = 10$ ). Only one source is active for each view.

### Inverse solver parameters

- Shared parameters

- Weight of the state term of the functional: 1.0;
- Weight of the data term of the functional: 1.0;
- Convergence threshold:  $10^{-10}$ ;
- Variable ranges:
  - \*  $\varepsilon_r \in [4.0, 6.2]$ ;
  - \*  $\Re\{E_{tot}^{int}\} \in [-8, 8]$ ,  $\Im\{E_{tot}^{int}\} \in [-8, 8]$ ;
- Degrees of freedom:
  - \* Considered frequency:  $f_{min} = 200$  [MHz],  $\lambda_b = 0.75$  [m];
  - \*  $\frac{(2ka)^2}{2} = \frac{\left(2 \times \frac{2\pi}{\lambda_b} \times \frac{L\sqrt{2}}{2}\right)^2}{2} = 4\pi^2 \left(\frac{L}{\lambda_b}\right)^2 = 4\pi^2 \left(\frac{0.8}{0.75}\right)^2 \simeq 44.87$ ;
- Number of cells:  $N = 49 = 7 \times 7$ ;
- Maximum number of *IMSA* steps:  $S = 4$ ;
- Side ratio threshold:  $\eta_{th} = 0.2$ ;

- *MF – IMSA – CG* parameters

- Maximum number of iterations:  $I = 200$ ;

- *FH – IMSA – CG* parameters

- Maximum number of iterations:  $I = 400$ ;

### Signal to noise ratio (on $E_{tot}(t)$ )

- $SNR = \{50, 40, 30, 20\}$  [dB] + Noiseless data.

**2.1.2  $\sigma_{obj} = 10^{-4}$  [S/m] ( $\Im\{\tau\} = 2.69 \times 10^{-2}$ ): Final reconstructions (@  $f_{max} = 600$  [MHz])**

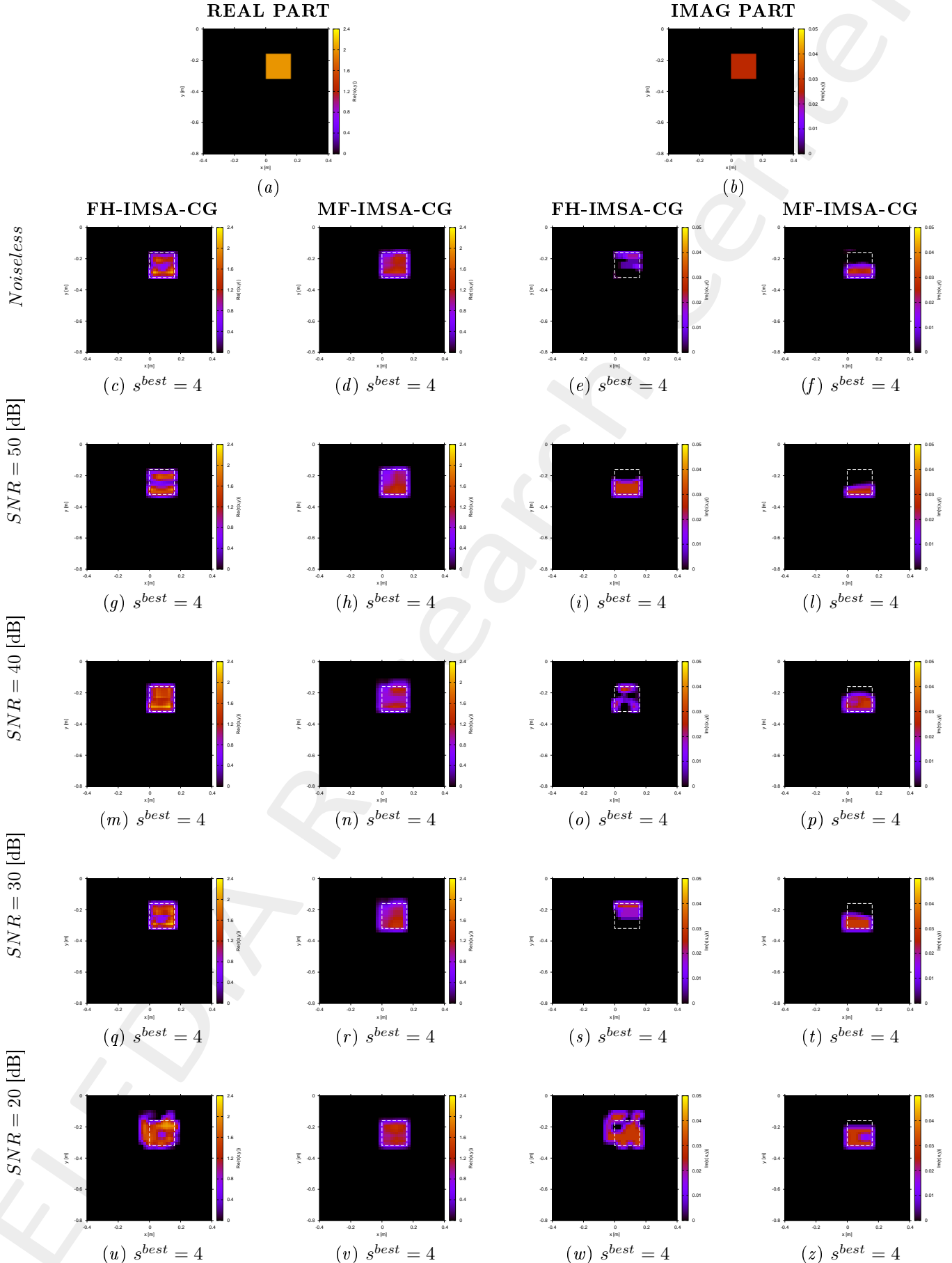


Figure 4: *FH – IMSA – CG* vs. *MF – IMSA – CG*: Retrieved dielectric profiles at the *IMSA* convergence step ( $s^{best}$ ).

**2.1.3**  $\sigma_{obj} = 5 \times 10^{-4}$  [S/m] ( $\Im\{\tau\} = 1.49 \times 10^{-2}$ ): Final reconstructions (@  $f_{max} = 600$  [MHz])

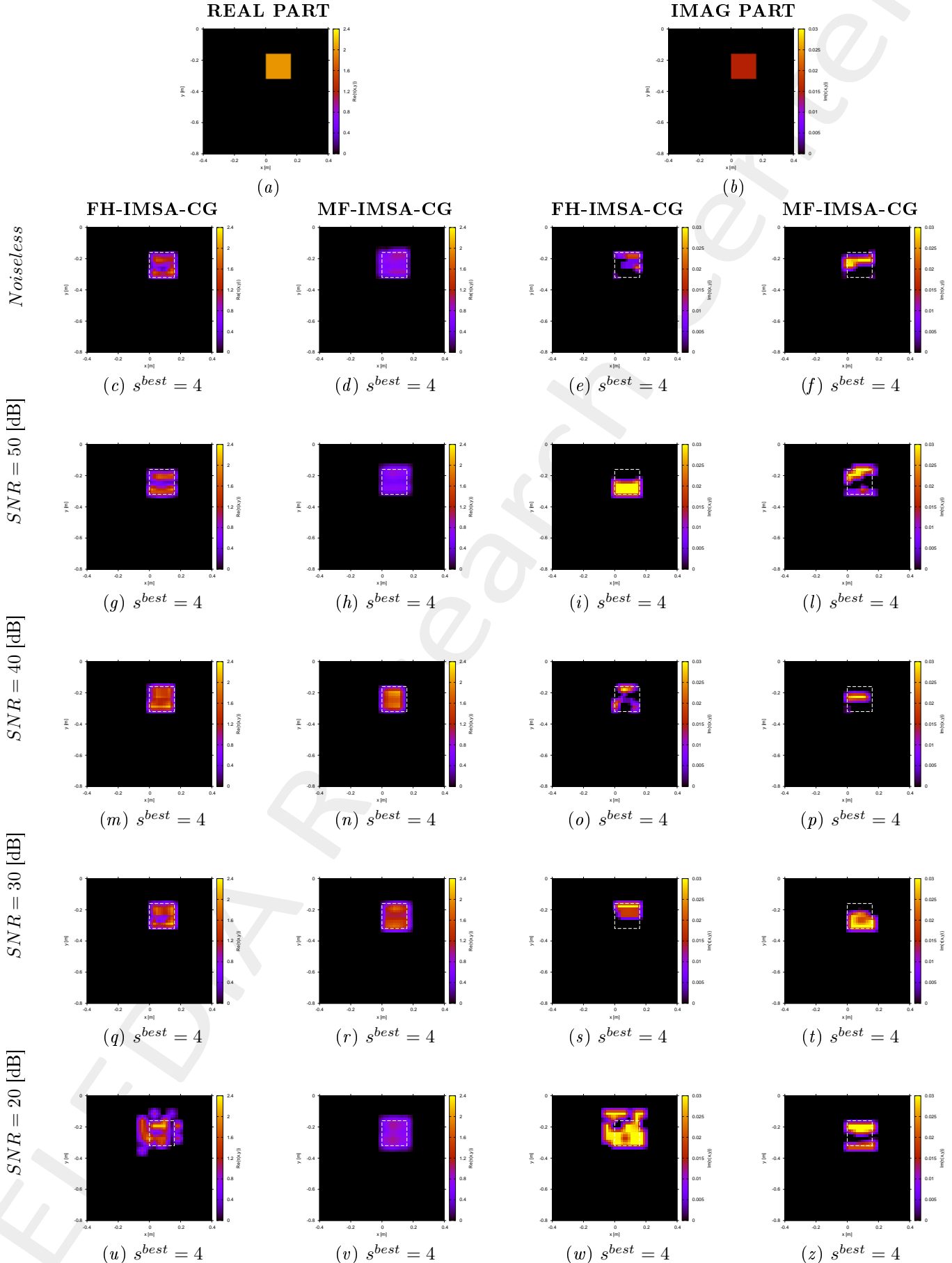


Figure 5:  $FH - IMSA - CG$  vs.  $MF - IMSA - CG$ : Retrieved dielectric profiles at the  $IMSA$  convergence step ( $s^{best}$ ).

**2.1.4  $\sigma_{obj} = 10^{-3}$  [S/m] ( $\Im\{\tau\} = 0.0$ ): Final reconstructions (@  $f_{max} = 600$  [MHz])**

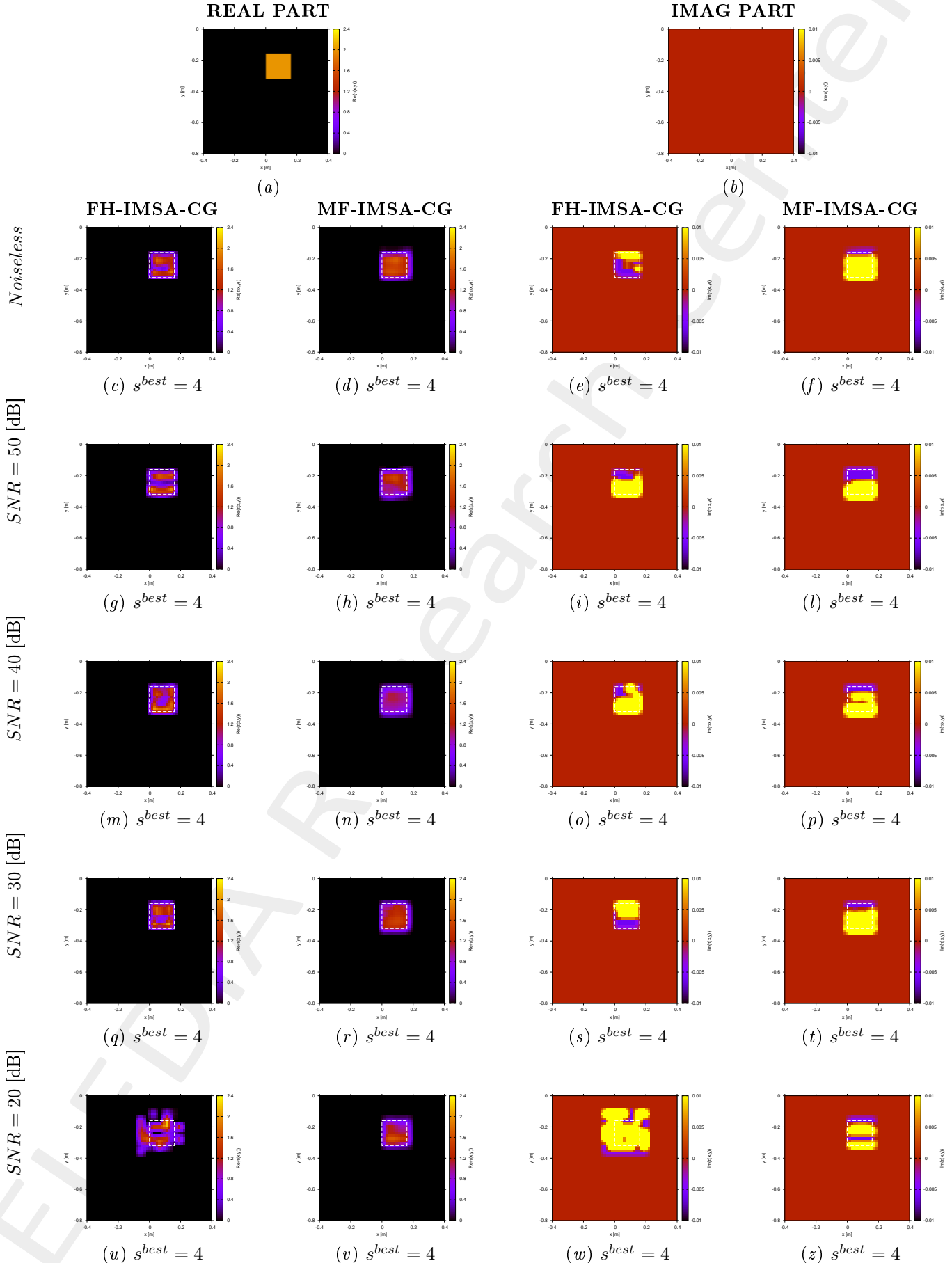


Figure 6:  $FH - IMSA - CG$  vs.  $MF - IMSA - CG$ : Retrieved dielectric profiles at the  $IMSA$  convergence step ( $s^{best}$ ).

**2.1.5**  $\sigma_{obj} = 5 \times 10^{-3}$  [S/m] ( $\Im\{\tau\} = -1.19 \times 10^{-1}$ ): Final reconstructions (@  $f_{max} = 600$  [MHz])

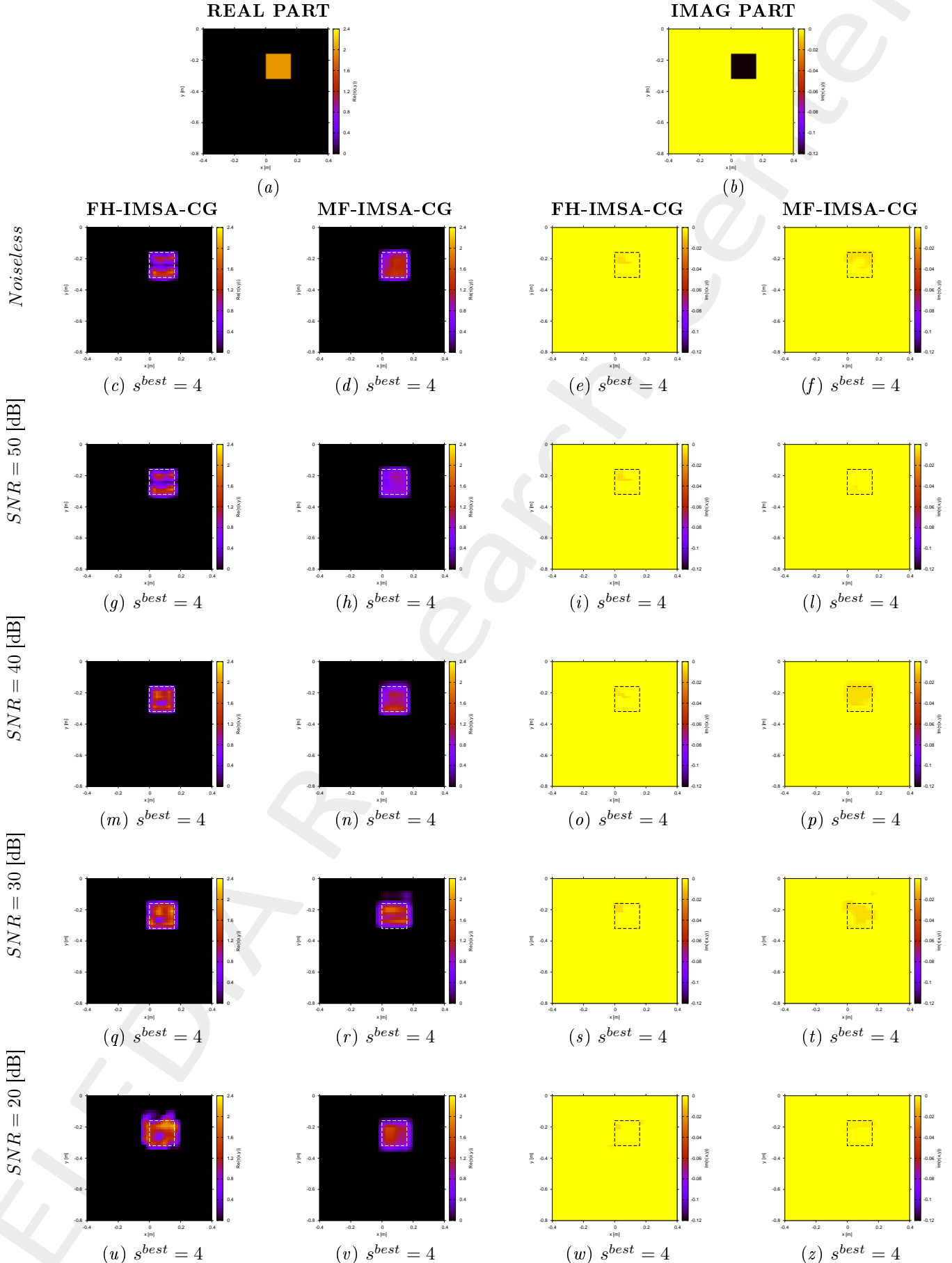


Figure 7:  $FH - IMSA - CG$  vs.  $MF - IMSA - CG$ : Retrieved dielectric profiles at the  $IMSA$  convergence step ( $s^{best}$ ).

### 2.1.6 Errors vs. $\sigma_{obj}$

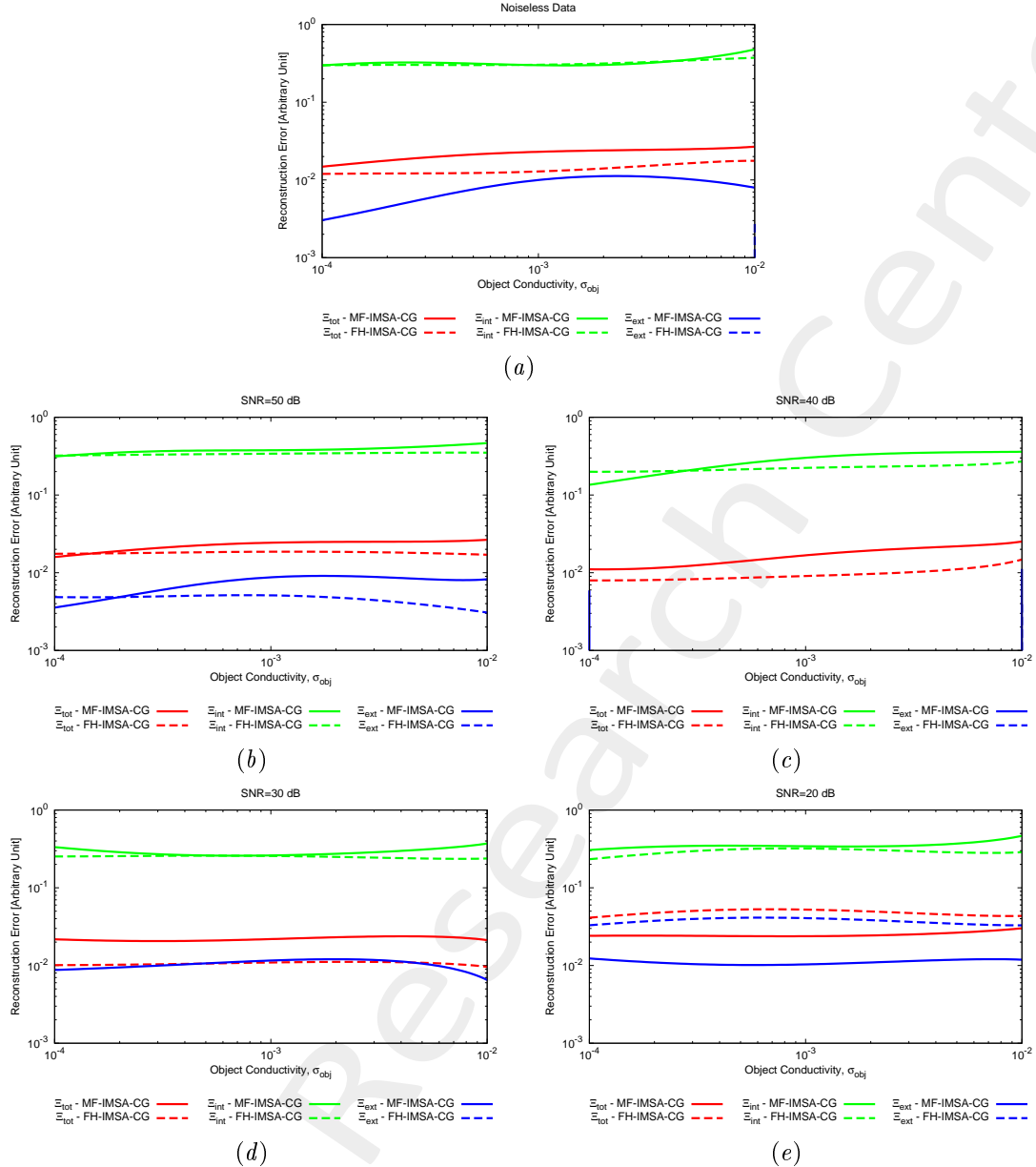


Figure 8:  $FH\text{-IMSA-CG}$  vs.  $MF\text{-IMSA-CG}$ : Reconstruction errors vs. the object conductivity ( $\sigma_{obj}$ ).

## References

- [1] P. Rocca, M. Benedetti, M. Donelli, D. Franceschini, and A. Massa, "Evolutionary optimization as applied to inverse problems," *Inverse Probl.*, vol. 25, pp. 1-41, Dec. 2009.
- [2] P. Rocca, G. Oliveri, and A. Massa, "Differential Evolution as applied to electromagnetics," *IEEE Antennas Propag. Mag.*, vol. 53, no. 1, pp. 38-49, Feb. 2011.
- [3] M. Salucci, G. Oliveri, and A. Massa, "GPR prospecting through an inverse scattering frequency-hopping multi-focusing approach," *IEEE Trans. Geosci. Remote Sens.*, vol. 53, no. 12, pp. 6573-6592, Dec. 2015.
- [4] M. Salucci, L. Poli, N. Anselmi and A. Massa, "Multifrequency particle swarm optimization for enhanced multiresolution GPR microwave imaging," *IEEE Trans. Geosci. Remote Sens.*, vol. 55, no. 3, pp. 1305-1317, Mar. 2017.
- [5] A. Massa, P. Rocca, and G. Oliveri, "Compressive sensing in electromagnetics - A review," *IEEE Antennas Propag. Mag.*, pp. 224-238, vol. 57, no. 1, Feb. 2015.
- [6] A. Massa and F. Texeira, Guest-Editorial: Special Cluster on Compressive Sensing as Applied to Electromagnetics, *IEEE Antennas Wireless Propag. Lett.*, vol. 14, pp. 1022-1026, 2015.
- [7] N. Anselmi, G. Oliveri, M. Salucci, and A. Massa, "Wavelet-based compressive imaging of sparse targets," *IEEE Trans. Antennas Propag.*, vol. 63, no. 11, pp. 4889-4900, Nov. 2015.
- [8] G. Oliveri, N. Anselmi, and A. Massa, "Compressive sensing imaging of non-sparse 2D scatterers by a total-variation approach within the Born approximation," *IEEE Trans. Antennas Propag.*, vol. 62, no. 10, pp. 5157-5170, Oct. 2014.
- [9] T. Moriyama, G. Oliveri, M. Salucci, and T. Takenaka, "A multi-scaling forward-backward time-stepping method for microwave imaging," *IEICE Electron. Expr.*, vol. 11, no. 16, pp. 1-12, Aug. 2014.
- [10] T. Moriyama, M. Salucci, M. Tanaka, and T. Takenaka, "Image reconstruction from total electric field data with no information on the incident field," *J. Electromagnet. Wave.*, vol. 30, no. 9, pp. 1162-1170, 2016.
- [11] F. Viani, L. Poli, G. Oliveri, F. Robol, and A. Massa, "Sparse scatterers imaging through approximated multi-task compressive sensing strategies," *Microw. Opt. Technol. Lett.*, vol. 55, no. 7, pp. 1553-1557, Jul. 2013.
- [12] M. Salucci, L. Poli, and A. Massa, "Advanced multi-frequency GPR data processing for non-linear deterministic imaging," *Signal Processing - Special Issue on 'Advanced Ground-Penetrating Radar Signal-Processing Techniques,'* vol. 132, pp. 306-318, Mar. 2017.
- [13] M. Salucci, N. Anselmi, G. Oliveri, P. Calmon, R. Miorelli, C. Reboud, and A. Massa, "Real-time NDT-NDE through an innovative adaptive partial least squares SVR inversion approach," *IEEE Trans. Geosci. Remote Sens.*, vol. 54, no. 11, pp. 6818-6832, Nov. 2016.

- [14] L. Poli, G. Oliveri, and A. Massa, "Imaging sparse metallic cylinders through a local shape function bayesian compressing sensing approach," *J. Opt. Soc. Am. A*, vol. 30, no. 6, pp. 1261-1272, Jun. 2013.